CHAPTER 4
NUMERICAL SIMULATION

4.1 Physical and Geometry Model

4.1.1 External Flow Geometry and Meshing Model

The numerical simulation for external flow domain utilized Ansys Fluent SpaceClaim as the tool to create the simulation domain. The simulation domain setup includes the velocity-inlet, container, pressure-outlet and the remaining channel surfaces defined as no-slip, adiabatic walls. Showing as in the Figure 4.1

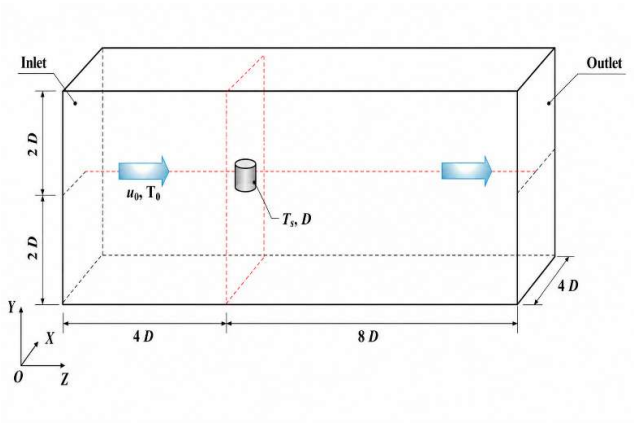

Figure 4.1 Simulation Domain of External Flow

Once the domain has been created, the next step is meshing. The computational domain for the external flow simulation was discretized using a polyhedral mesh, selected for its superior cell quality on complex geometries compared with conventional tetrahedral elements, as well as its ability to reduce the overall cell count without compromising solution accuracy. This consideration is particularly important given that the Large Eddy Simulation (LES) approach adopted in this study already demands high spatial resolution combined with a substantial computational cost arising from its inherently time-accurate nature.

The meshing strategy was divided into two principal regions: the mainstream region, covering the bulk flow domain surrounding the sphere, and the near-surface region, where the boundary layer develops along the sphere surface. An inflation layer was applied near the sphere surface to resolve the developing boundary layer, an essential requirement for LES since an under-resolved boundary layer forces the

sub-grid scale model to compensate for turbulent kinetic energy that should otherwise be directly resolved, degrading the accuracy of the predicted Nu. The inflation growth was configured using the Last Ratio (Last Aspect Ratio) method, in which the first prism layer height is explicitly prescribed and subsequent layers expand at a defined growth rate until reaching the aspect ratio of the surrounding mainstream mesh. This method was chosen for its direct control over the first-layer height, the parameter most critical to boundary layer resolution, unlike the Total Thickness method, which constrains only the cumulative inflation thickness without guaranteeing adequate resolution of the first near-wall cell.

$$\delta_{BL} = \frac{1{,}13.d_c}{\sqrt{Re}} \tag{4.1}$$

where δ_{BL} denotes the momentum boundary layer thickness, d_c the container diameter, and Re the Reynolds number corresponding to the simulated flow condition. This correlation provides a conservative estimate of the boundary layer thickness at the stagnation point, which was subsequently used as the basis for sizing the first prism layer. Showing as in the Figure 4.2

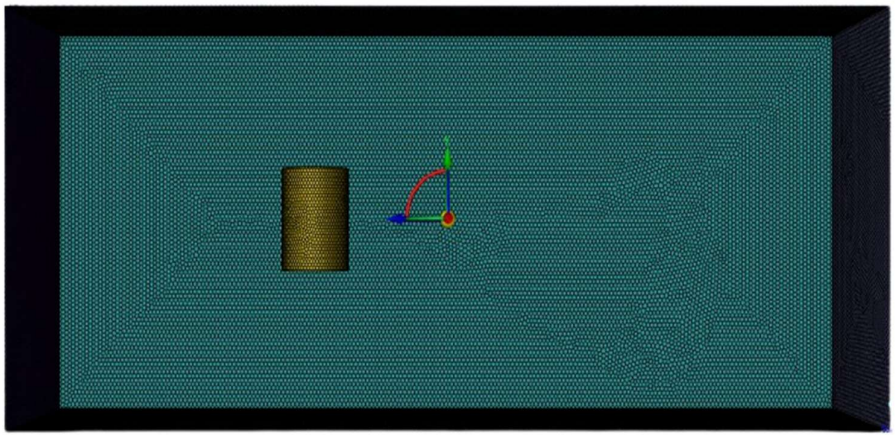

Figure 4.2 External Flow Meshing

4.1.2 PCM melting Geometry and Meshing Model

The computational domain for the PCM melting simulation was created using Ansys SpaceClaim. Since this domain represents an enclosed system without flow inlet or outlet, it consisted solely of the PCM region bounded by the container wall,

which was defined as a constant-temperature wall boundary condition to drive the melting process. Showing as in the Figure 4.3

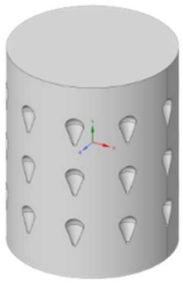

Figure 4.3 PCM Melting Object

Unlike the external flow simulation, which required strict boundary layer resolution due to the forced-convection nature of the high-Reynolds-number flow, the PCM melting simulation inside the cylindrical container involves a laminar flow regime at considerably lower velocities, driven primarily by natural convection arising from buoyancy forces represented through the Boussinesq approximation. Consequently, the meshing strategy for the internal PCM domain did not rely on a boundary-layer correlation-based inflation approach as used in the external case. Instead, emphasis was placed on maintaining a sufficiently fine and uniform resolution throughout the domain, capable of accurately capturing the movement of the melting front as well as the natural convection circulation patterns that develop within the liquid PCM. Showing as in the Figure 4.4

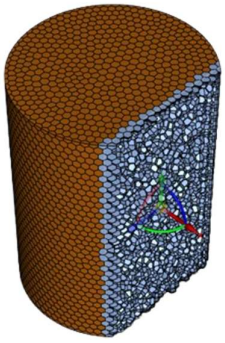

Figure 4.4 PCM Melting Meshing

4.2 Governing Equation

4.2.1 External Flow Equation

The external flow simulation in this study was solved using the Large Eddy Simulation (LES) approach, in which the turbulent flow field is decomposed through spatial filtering into a resolved component, representing large-scale eddies computed directly by the grid, and a sub-grid scale (SGS) component, representing small-scale eddies below the filter width that must be model. The corresponding continuity, momentum, and energy equations solved under this approach are presented in Equations (4.2) through (4.4):

Conitnuity Equation:

$$\frac{\partial p}{\partial t} + \frac{\partial}{\partial x_i}(\rho u_i) = 0 \tag{4.2}$$

Where $\frac{\partial p}{\partial t}$ denotes as the rate of change of fluid density with respect to time at a fixed point, $\frac{\partial}{\partial x_i}(\rho u_i)$ as spatial divergence of mass flux, representing the net mass flow rate per unit volume leaving the control volume.

Momentum Equation:

$$\frac{\partial}{\partial t}(\rho \bar{u_\iota}) + \frac{\partial}{\partial x_j}\left(\rho \bar{u_\iota} \bar{u_J}\right) = \frac{\partial}{\partial x_j}\left(\bar{\sigma}_{ij}\right) - \frac{\partial \bar{p}}{\partial x_i} - \frac{\partial \tau_{ij}}{\partial x_j} \tag{4.3}$$

Where $\rho \bar{u_\iota}$ denotes as the transient rate of change of the filtered momentum, $\rho \bar{u_\iota} \bar{u_J}$ is the convective transport term against the forces acting on the fluid, $\bar{\sigma}_{ij}$ is the viscous stress tensor, $-\frac{\partial \bar{p}}{\partial x_i}$ is the filtered pressure gradient, and τ_{ij} is the sub-grid scale turbulent stress. τ_{ij} in LES represents only the smallest, most universal and near-isotropic scales of turbulence.

This distinction is what allows LES to resolve unsteady flow structures such as vortex shedding directly, rather than modeling them statistically, giving LES a clear advantage over RANS for capturing the transient wake dynamics.

Energy Equation :

$$\frac{\partial T}{\partial t} + \frac{\partial}{\partial x_j}\left(T \bar{u_J}\right) = \frac{\partial}{\partial x_j}\left[(\alpha + \alpha_{SGS})\frac{\partial T}{\partial x_j}\right] \tag{4.4}$$

Where α represnets the molecular thermal diffusivity , α_{SGS} is the sub-grid thermal diffusivity. This equation directly produces the resolved temperature distribution around the container surface, from which the local and average Nusselt number are subsequently evaluated.

For τ_{ij} in Equation (4.3) is not directly known, it must be modeled through a closure relation. Where represent by Equation 4.5 below :

Sub-grid scale stress closure (Boussineq hypothesis) :

$$\tau_{ij} + \frac{1}{3}\tau_{kk}\delta_{ij} = -2\mu_{t,sub}\bar{S}_{ij} \tag{4.5}$$

Where the term τ_{ij} represents the unknown sub-grid scale (SGS) turbulent stress tensor, while τ_{kk} denotes the isotropic part (trace) of this stress tensor, and δ_{ij} is the kronecker delta. Additionally, $\mu_{t,sub}$ signifies the sub-grid scale turbulent viscosity, $\bar{S}_{ij}$ refers to the rate of strain tensor for the resolved scales, which describes the local deformation rate of the filtered flow field.

To evaluate $\mu_{t,sub}$, Smagorinsky-lily model used to provide specific formulation. Showing in the Equation 4.6

Smagorinsky-lily Model Equation:

$$\mu_t = pL_s^2\sqrt{2\bar{S}_{ij}\bar{S}_{ij}} \tag{4.6}$$

Where μ_t is the sub-grid scale turbulent viscosity, which is essential for closing momentum equation in large eddy simulation, p is the fluid density, L_s is the mixing length of the sublatice scale, and $\bar{S}_{ij}$ signifies as the rate of strain tensor for the resolved scales, which describes the local deformation rate of filtered flow field.

4.2.2 Phase Change Internal (PCM Melting)

The melting behavior of the phase change material (PCM) within the enclosure is modeled using the enthalpy–porosity method, a widely adopted numerical approach for solid–liquid phase transition problems that avoids explicit tracking of the moving solid–liquid interface. This formulation enables the solution of the governing conservation equations on a single constant computational domain

throughout the solid, mushy, and liquid phases by treating the mushy (transition) region as a pseudo-porous medium whose porosity varies continuously with the local liquid fraction. The following are the governing equations for the transport of mass, momentum, and energy during melting. Showing in the Equation 4.7 through 4.12

Continuity Equation:

$$\frac{\partial p}{\partial t} + \frac{\partial}{\partial x_i}(\rho u_i) = 0 \tag{4.7}$$

Where $\frac{\partial p}{\partial t}$ denotes as the rate of change of fluid density with respect to time at a fixed point, $\frac{\partial}{\partial x_i}(\rho u_i)$ as spatial divergence of mass flux, representing the net mass flow rate per unit volume leaving the control volume. This equation applies uniform mass conservation throughout the solid, liquid, and mushy areas of the PCM domain, treating them as a continuous continuum.

Momentum Equation:

$$\frac{\partial}{\partial t}(\rho\overline{u_\iota}) + \frac{\partial}{\partial x_j}\left(\rho\overline{u_\iota}\overline{u_\jmath}\right) = -\frac{\partial \bar{p}}{\partial x_i} - \frac{\partial^2 u_i}{\partial x_j \partial x_j} + \rho g_i\left[1 - \beta\left(T - T_{ref}\right)\right] + S(T)u_i \tag{4.8}$$

Where $\rho g_i\left[1 - \beta\left(T - T_{ref}\right)\right]$ applies the boussineq approximation, β as the thermal expansion coefficient, representing the net mass flow rate per unit volume leaving the control volume. This equation applies uniform mass conservation throughout the solid, liquid, and mushy areas of the PCM domain, treating them as a continuous continuum. $S(T)u_i$ is a momentum sink/source term that forces the velocity toward zero within fully solid regions while allowing unrestricted flow in fully liquid regions, providing the mechanism by which phase transition is represented without an explicit interface-tracking algorithm.

Energy Equation (entalphy form):

$$\frac{\partial(pH)}{\partial t} + \frac{\partial}{\partial x_i}(\rho u_i H) = \frac{\partial}{\partial x_i}\left(k\frac{\partial T}{\partial x_i}\right) \tag{4.9}$$

Where H is the total enthalphy that solved initially rather than temperature directly. This formulation avoids the need to explicitly locate and track the moving melting front at every time step.

Momentum Source Term Equation:

$$S(T) = -A_{mush}\frac{(1-\theta(T))^2}{\theta(T)^3+\varepsilon} \tag{4.10}$$

Where $\theta(T)$ is the liquid fraction, $-A_{mush}$is the mushy zone constant that controls the steepness of the velocity supress, while ε is a small constant introduced solely to prevent division by zero when $\theta = 0$.

Liquid Fraction Equation :

$$\theta(T) = \begin{cases} 0, & T < T_m - \frac{\Delta T}{2} \\ \frac{T-\left(T_m-\frac{\Delta T}{2}\right)}{\Delta T}, & T_m - \frac{\Delta T}{2} < T < T_m + \frac{\Delta T}{2} \\ 1, & T > T_m - \frac{\Delta T}{2} \end{cases} \tag{4.11}$$

Where $T_m - \frac{\Delta T}{2}$ is the solidus temperature and $T_m + \frac{\Delta T}{2}$ is the liquidus temperature, compared to more complex non-linear liquid fraction models, this linear approximation provides a computationally efficient option.

Enthalphy Equations:

$$H = h + \Delta H,\ h = h_{ref} + \int_{T_{ref}}^{T} C_p dT,\ \Delta H = \theta(T)L \tag{4.12}$$

Where in this equation, the total enthalpy into a sensible component h, associated with pure temperature change, and a latent component ΔH, associated with the absorption or release of latent heat during phase transition, scaled directly by the liquid fraction $\theta(T)$ and the total latent heat of fusion L.

4.3 Boundary Condition

4.3.1 External Flow

1. Upstream boundary of the domain was assigned a velocity inlet condition, with the freestream velocity $u_0$varied according to the three Reynolds numbers investigated in this study (500,2500 and 5000), while the inlet temperature was held constant at $T_0 = 298$K.
2. To represent a low-disturbance freestream condition consistent with the setup adopted by Jia et al. (2024)[7], turbulence intensity at the inlet was fixed at 0.5%.

3. Downstream boundary of the domain was set as a pressure outlet with zero-gauge pressure, allowing the flow to exit the domain freely without imposing an artificial pressure gradient.
4. No-slip condition together with a fixed surface temperature of $T_s = 318\text{K}$ was imposed on the sphere surface, representing the heated boundary responsible for convective heat exchange with the surrounding air.
5. Surrounding channel walls, meanwhile, were defined as no-slip and adiabatic, so that heat transfer would occur solely through the sphere surface rather than through the domain boundaries.
6. Reference area and reference length adopted by the solver for computing convective heat transfer coefficient. For the smooth cylinder the reference area is 0,0141m^2 and for the dimpled cylinder is 0.01474 m^2.

4.3.2 Phase Change Internal (PCM melting)

1. Container wall was modeled as a no-slip, constant-temperature boundary utilized $T_s = 318$ K at the wall_heat for the smooth and dimpled container.
2. The mushy zone constant, A_{mush} , which governs the steepness of the velocity suppression as the PCM transitions from liquid to solid was set to 1e+6, a value commonly adopted in enthalpy-porosity based melting simulations to ensure that the velocity within fully solid regions is effectively forced toward zero.
3. Throughout the PCM domain, the initial temperature was set uniformly below the melting point T_m, corresponding to a fully solid state at t=0.
4. Velocity field across the entire domain was likewise initialized at zero, in line with the stationary, fully solid condition of the PCM prior to heating.
5. In contrast to the external flow domain, no inlet or outlet boundary was defined for the PCM domain, since it remains fully enclosed and involves no external mass flow throughout the melting process.
6. Gravitational acceleration was activated and oriented in accordance with the physical orientation of the cylindrical container, given its direct role in driving the buoyancy-induced natural convection term within the momentum equation.

7. Dimpled region of the container surface was assigned the same constant-temperature wall condition as the rest of the container wall, so that the dimple structure functions purely as a geometric modification rather than introducing a separate thermal boundary condition.

4.4 Solution Process

Governing equations solved in the external flow simulation, comprising the filtered continuity, momentum, and energy equations under the Large Eddy Simulation framework, were resolved using the pressure based solver in ANSYS Fluent. Pressure velocity coupling was handled through the PISO (Pressure Implicit with Splitting of Operators) algorithm, selected over the conventional SIMPLE scheme owing to its superior stability and accuracy for transient, time accurate simulations such as those required by LES. Pressure interpolation was carried out using the PRESTO! (PREssure STaggering Option) scheme, chosen for its capability to accurately resolve steep pressure gradients arising from the strong flow curvature and separation around the bluff body surface, conditions under which standard or linear pressure interpolation schemes tend to lose accuracy. Spatial discretization of the convective terms in the momentum equation was carried out using a Bounded Central Differencing (BCD) scheme, chosen for its low numerical dissipation and its suitability for resolving the fine scale turbulent structures inherent to LES, while temporal discretization was performed using a Second Order Implicit (SOI) formulation to maintain accuracy across successive time steps.

Simulation was advanced iteratively in a transient manner until a statistically stationary flow condition was reached, rather than a single steady state solution. Convergence at each time step was assessed by monitoring the scaled residuals of the continuity and momentum equations, with a threshold of below 10^{-3} adopted as the convergence criterion, while a stricter threshold of below 10^{-6} was applied to the energy equation given its greater sensitivity in capturing accurate thermal predictions. Beyond residual monitoring, time histories of convective heat transfer coefficient was tracked throughout the simulation to confirm that this quantities had reached a statistically stable, time periodic pattern, offering a more physically

meaningful indicator of solution convergence than residual values alone, particularly given the inherently fluctuating nature of the resolved turbulent wake.

Once the external flow simulation had been validated, the internal phase change process was subsequently examined using the enthalpy-porosity method under a separate transient solver configuration. Within this framework, the momentum source term governing the mushy zone resistance was iterated at every time step alongside the coupled continuity, momentum, and energy equations until convergence of the liquid fraction field was achieved, ensuring that the solid liquid interface evolution had been fully resolved before the solution advanced to the subsequent time step. The same residual convergence criteria applied to the external flow simulation, namely below 10^{-3} for continuity and momentum and below 10^{-6} for energy. were adopted throughout this simulation.

4.5 Mesh Independence Test

4.5.1 External Flow

To ensure that the numerical results obtained for the cylindrical container geometry were not influenced by mesh resolution, a mesh independence test was carried out prior to conducting the main simulations. Following the two-stage strategy applied throughout this study, the test was performed separately for the mainstream region, covering the bulk flow domain surrounding the cylinder, and the cylinder surface region, where the boundary layer develops. Showing in the Figure 4.5

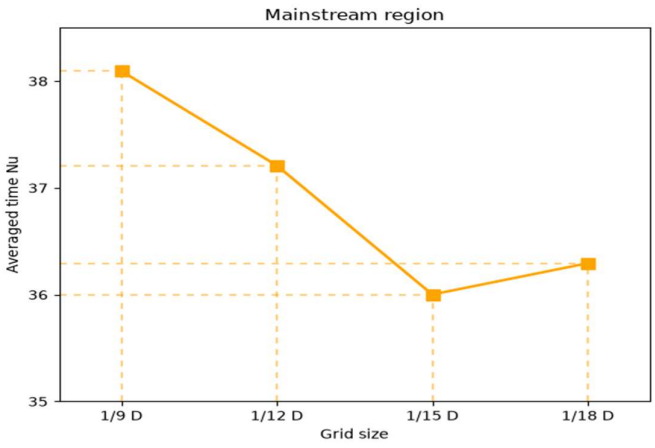

(a)

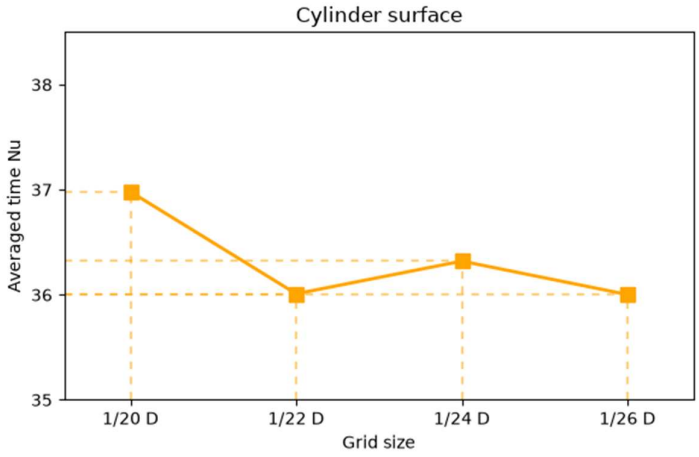

(b)

Figure 4.5 Mesh Independency Test (a) Mainstream Region (b) Cylinder Surface

Four progressively refined element sizes were evaluated for the mainstream region: 1/9D, 1/12D, 1/15D, and 1/18D. As presented in Figure 4.4a, the Nusselt number decreased from 38.1 at 1/9D to 37.2 at 1/12D, corresponding to an error of 2.362%, and further decreased to 36.0 at 1/15D, yielding a larger error of 3.226%. Upon further refinement to 1/18D, the Nusselt number changed only marginally to 36.3, corresponding to an error of 0.833%. Since this error fell below the 1% threshold adopted as the convergence criterion in this study, the mesh with an element size of 1/15D was selected for the mainstream region, as further refinement to 1/18D produced no meaningful improvement in accuracy while having additional computational cost.

A similar procedure was applied to the cylinder surface region as presented in Figure 4.4b, with element sizes ranging from 1/20D to 1/26D. The Nusselt number decreased from 36.980 at 1/20D to 36.009 at 1/22D, corresponding to an error of 2.626%. Upon further refinement to 1/24D, the Nusselt number increased slightly to 36.320, yielding a considerably smaller error of 0.864%, followed by a further change to 36.002 at 1/26D, with an error of 0.876%. Since the error dropped below the 1% threshold beginning at the transition from 1/22D onward, the element size of 1/22D was selected as the mesh independent resolution for the cylinder surface region.

4.5.2 Phase Change Internal (PCM Melting)

Mesh independency test in the melting simulation was assessed differently from the external flow case. Instead of using a single time-averaged value, the comparison was made by observing the full liquid fraction curve over time, since this variable shows the entire melting progress and is more sensitive to mesh-related error than a single data point. Four mesh configurations with increasing refinement, namely 1/10D, 1/21D, 1/25D, and 1/30D, were compared for this purpose, with the resulting curves showing in the Figure 4.6 below.

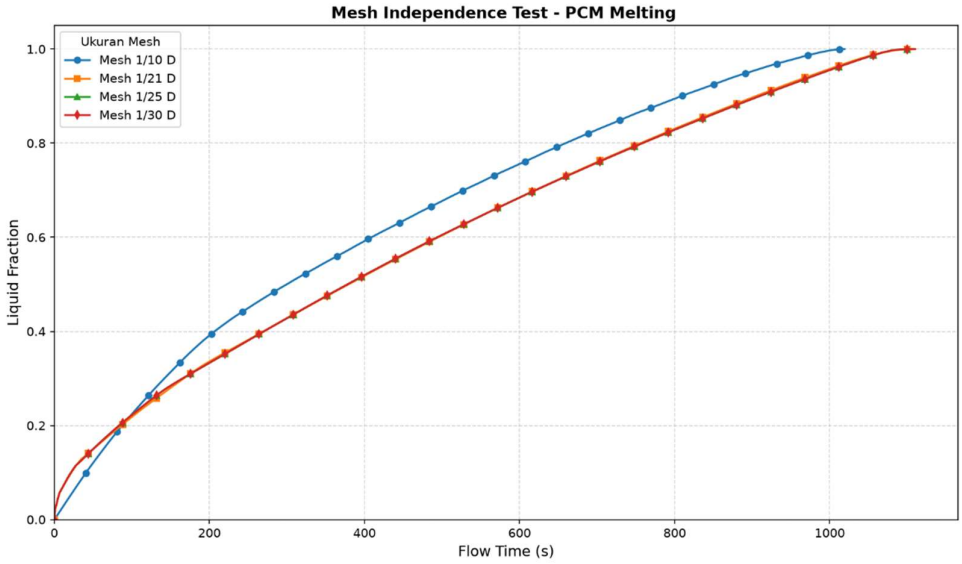

Figure 4.6 Mesh Independency Test of Phase Change Internal

Throughout the simulation, the liquid fraction curve for the mesh 1/10D, remained above the other three curves and reach complete melting much earlier. This shows the mesh not fine enough, especially near the container wall and in growing liquid region, where the temperature change rapidly due to natural convection.

Meshes of 1/21D, 1/25D, and 1/30D, by comparison, produced liquid fraction curves that overlapped almost completely across the entire flow time range, from the initial stage of melting through to full phase transition. This near-total agreement among the three finer meshes, without any meaningful separation between them at any point along the curve, provided strong evidence that further

refinement beyond 1/21D no longer altered the predicted melting behavior. Element size of 1/21D was adopted for the PCM melting simulation, offering a solution effectively identical from the two finer alternatives while demanding considerably less computational effort.

4.6 Time Step Verification

4.6.1 External Flow

In addition to the mesh independence test, a time step verification was also carried out prior to running the main simulations, since the LES approach adopted in this study is transient in nature and therefore highly sensitive to temporal resolution. Four dimensionless time step values were evaluated, namely 0.01, 0.015, 0.02, and 0.03, with the time-averaged Nusselt number used as the comparison parameter. Alongside this, the Courant-Friedrichs-Lewy (CFL) number was also calculated for each case to confirm that numerical stability was maintained throughout the verification process.

The CFL number is a dimensionless parameter representing how far a fluid quantity travels across a computational cell within a single time step. Showing in the Equation 4.13

$$CFL = \frac{u\Delta t}{\Delta x} \tag{4.13}$$

where u u is the local flow velocity, Δt is the time step size, and Δx is the local cell size along the flow direction. A CFL value greater than one indicates that fluid information moves further than one computational cell within a single time step, which can lead to numerical instability or divergence, particularly for explicit solution schemes. For this reason, a CFL value below one is generally regarded as a safe stability limit, ensuring that information transport remains confined within a single cell per time step. Shwoing in the Figure 4.7 and Table 4.1

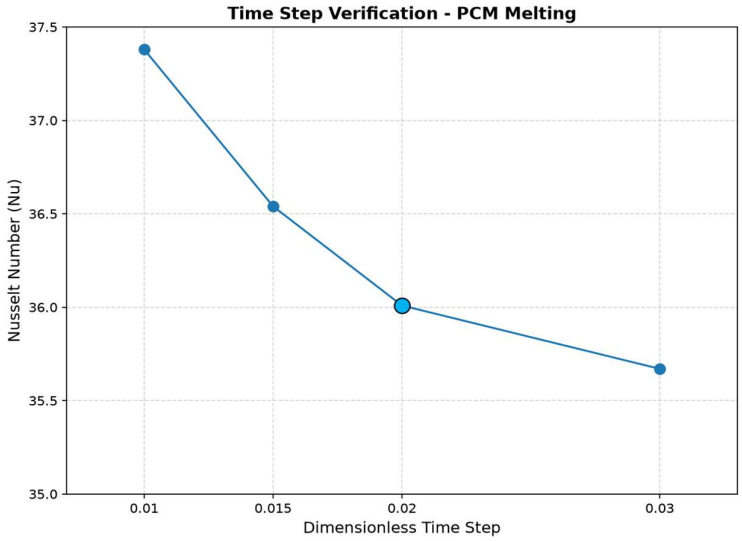

Figure 4.7 Time step Verification for External Flow

Table 4.1 Time Step Verification

Time step verification			
Dimensional time step	Time step size	Cfl	Nu
0,01	0,034	0,22	37,38
0,015	0,051	0,33	36,54
0, 02	0,068	0,44	36,009
0,03	0,1027	0,66	35,67

The resulting Nusselt number together with the corresponding CFL value for each dimensionless time step is summarized in Table 4.x. Across all four cases, the CFL number remained below one, ranging from 0.22 to 0.66, confirming that numerical stability was preserved throughout the entire range tested. Error began to drop below the 1% threshold near the transition from 0.02 to 0.03, indicating that the solution had started to stabilize within this range.

Based on this observation, a dimensionless time step of 0.02 was selected for all subsequent simulations. This choice was made for two main reasons: first, the corresponding CFL value of 0.44 provided a comfortable safety margin below the stability limit; second, this time step offered finer temporal resolution compared to 0.03, which was considered important for accurately capturing the vortex shedding behavior inherent to the LES approach, while still remaining computationally more efficient than the smaller time steps of 0.01 and 0.015.

4.6.2 Phase Change Internal

Four time step sizes were therefore evaluated directly based on the resulting total flow time required to reach complete melting, namely 0.3, 0.5, 0.7, and 1. Showing as in the Figure 4.8

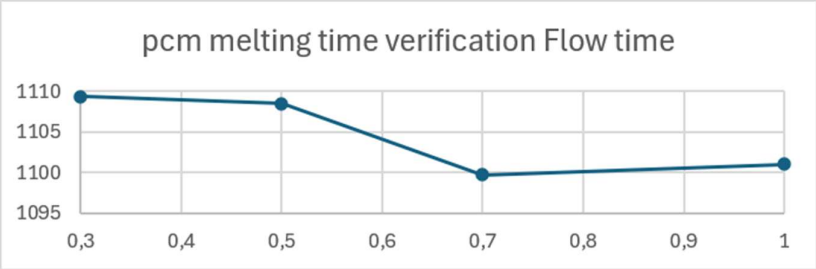

Figure 4.8 Time step Verification for Phase Change Internal

As shown in Figure 4.7, the total flow time required for complete melting was 1109.4 at a time step size of 0.3, decreasing slightly to 1108.5 at 0.5, followed by a further decrease to 1099.7 at 0.7, before increasing again to 1101 at a time step size of 1. The variation among all four time step sizes remained small, with the largest change occurring between 0.5 and 0.7. The slight increase observed at the largest time step, 1, rather than a continued decrease, suggests that the solution had already reached a stable range and that further coarsening introduced only minor numerical scatter rather than a systematic trend.

Based on this comparison, a time step size of 0.5 was selected for the PCM melting simulation. This value produced a result nearly identical to the finest time step tested (0.3), with a difference of less than 0.1%, while requiring fewer time steps to complete the simulation, thereby offering a practical balance between solution accuracy and computational efficiency.

4.7 Validation

Prior to investigating the flow and heat transfer characteristics of the dimpled cylindrical container, the numerical model developed in this study was first validated against the work of Jia et al. (2024), covering both the external flow and internal melting simulations. Since the reference dataset itself was previously verified against the Ranz-Marshall and Whitaker correlations and the CFD benchmark of Dixon et al. (2011), reproducing it and achieving close agreement

provides a reliable basis for trusting the present model. These results establish a solid baseline for evaluating the dimpled container in the following sections.

4.7.1 External Flow Validation

This validation case reconstructed their spherical capsule geometry (D = 21 mm) enclosed within a 4D × 4D square channel, with water simulated across Reynolds numbers ranging from 818 to 4908, following the same boundary conditions and parameters used in their study. Showing in the Figure 4.9

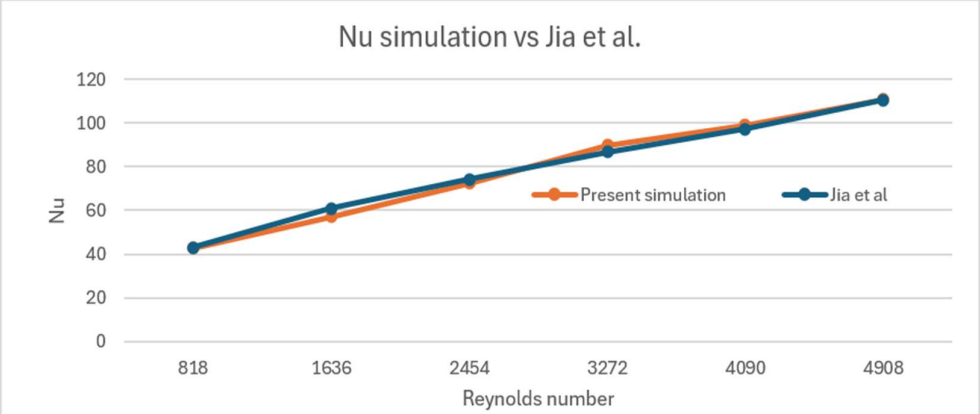

Figure 4.9 Nu simulation vs Jia et al

For the external flow, time-averaged Nusselt number , was compared against the smooth sphere results of Jia et al. (2024)[7]. As shown in Figure 4.8, both curves followed a closely matching trend across the full Reynolds number range, yielding an average deviation of 2.54%, confirming that the mesh, Smagorinsky-Lilly sub-grid model, and boundary conditions adopted here correctly captured the external convective heat transfer behavior.

4.7.2 Phase Change Internal Validation

For the internal phase-change process, the transient liquid fraction was compared against the same reference over the full melting duration. The two curves tracked one another closely from onset to near-complete melting, with only a slight lag in the mid-melting stage, giving an average deviation of 7.06%, an acceptable margin given the additional numerical sensitivity of the enthalpy-porosity method. Showing in the Figure 4.10

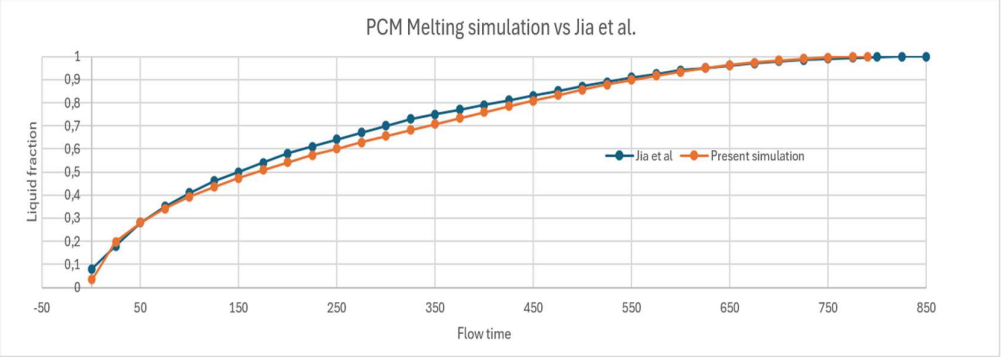

Figure 4.10 Liquid Fraction Simulation vs Jia et al

4.8 Simulation Result

4.8.1 External Flow Result

4.8.1.1 Temperature contour and velocity streamline

a. Re 500

This section explains the temperature contour and velocity streamline for smooth and dimpled cylindrical container at Re 500. Showing in the Figure 4.11

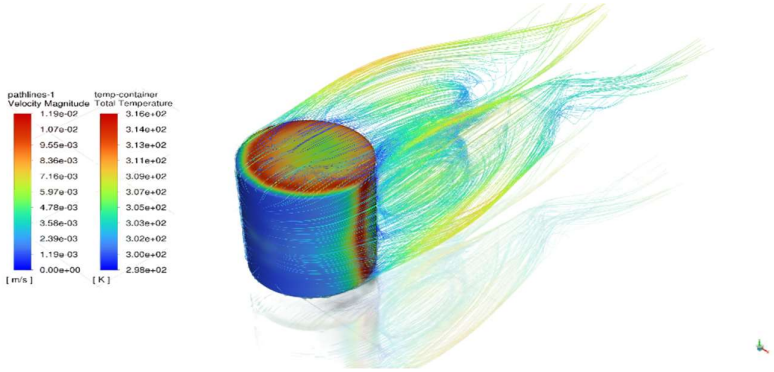

(a)

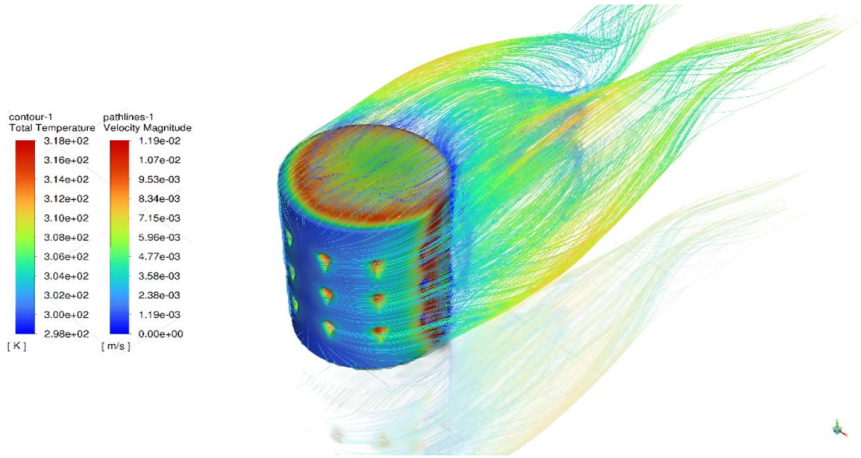

(b)

Figure 4.11 Temperature Contour and Velocity Streamline at Re 500 (a) Smooth Cylinder, (b) Dimpled Cylinder

Figure 4.9 presents velocity pathlines and total temperature contours for the smooth (a) and teardrop-dimpled (b) cylindrical containers at Re = 500. For the smooth container, the pathlines show largely attached, orderly flow along the surface before separating near the rear edge into a single coherent wake. The temperature contour reveals a thin, well-defined thermal boundary layer, with peak temperature reaching approximately 316 K concentrated near the front and side, where attached flow continuously sweeps heated fluid away before it accumulates.

For the dimpled container, the pathlines show a markedly different behavior, instead of sweeping past the surface, flow enters each dimple cavity and forms small, closed recirculating loops trapped within the pocket, where local velocity drops close to zero. This matches the temperature contour, where fluid inside the dimples reaches a higher peak of approximately 318 K and appears less diluted than the surrounding surface, indicating that heated fluid is retained locally rather than exchanged with the cooler freestream.

This behavior reflects the dead zone phenomenon commonly reported for dimpled surfaces at low Reynolds numbers. Dimple-induced enhancement normally relies on incoming flow momentum being strong enough to eject fluid from the cavity and re-energize the boundary layer. At Re = 500, momentum is

insufficient for this ejection, so the trapped vortex instead behaves as a stagnant, insulating pocket rather than a mixing mechanism. Since heat transfer coefficient depends directly on the wall temperature gradient, this retained heated layer reduces that gradient, explaining why the dimpled container yielded a lower area-averaged heat transfer coefficient than the smooth one at this Reynolds number.

b. Re 2500

This section explains the temperature contour and velocity streamline for smooth and dimpled cylindrical container at Re 2500. Showing in the Figure 4.12

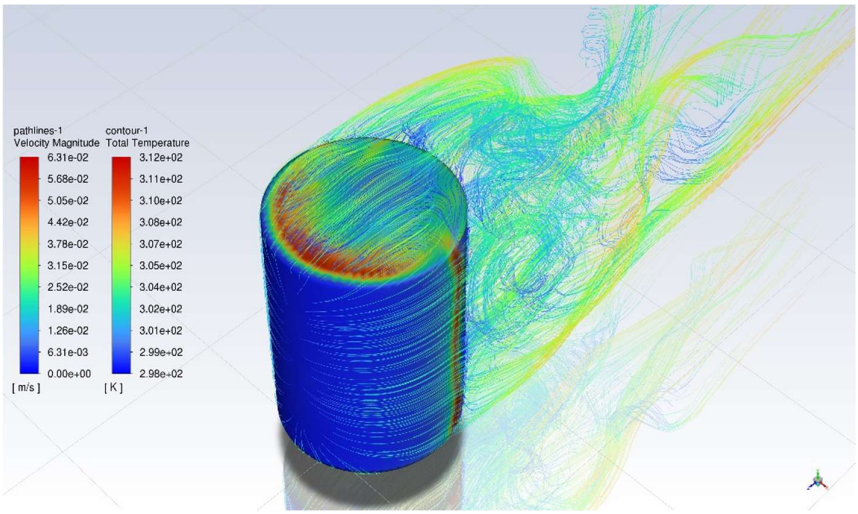

(a)

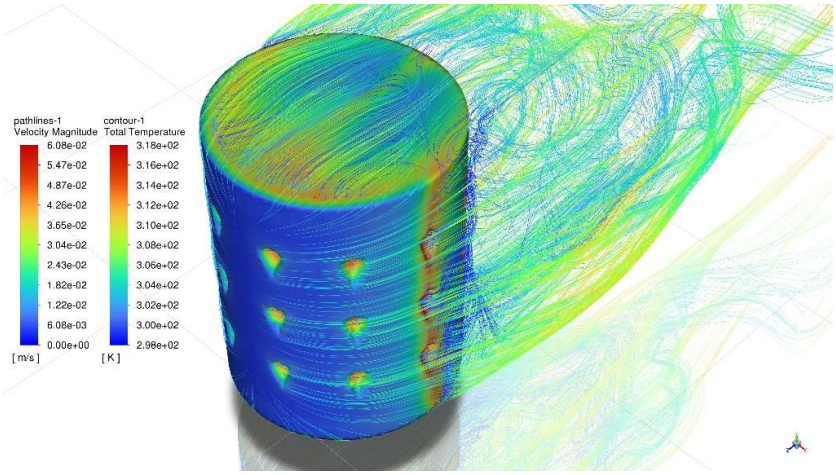

(b)

Figure 4.12 Temperature Contour and Velocity Streamline at Re 2500(a) Smooth Cylinder, (b) Dimpled Cylinder

Figure 4.10 presents velocity pathlines and total temperature contours for the smooth (top) and teardrop-dimpled (bottom) cylindrical containers at Re = 2500. For the smooth container, the wake appears considerably more chaotic than at Re = 500, with overlapping swirling filaments extending downstream rather than forming a single coherent recirculation loop, reflecting the onset of active vortex shedding at this higher momentum. The temperature contour shows a fairly uniform thermal boundary layer, with peak temperature reaching around 312 K, suggesting that the stronger flow continues to sweep heated fluid away from the wall efficiently.

For the dimpled container, the pathlines show a distinctly different pattern compared to the closed, trapped vortices observed at Re = 500. Instead of remaining confined within each cavity, the flow now forms jet-like structures ejecting outward from the dimples into the surrounding stream, reaching velocity magnitudes comparable to the freestream. The temperature contour correspondingly shows the highest local temperature, around 318 K, concentrated at the dimple locations, though this heated fluid appears to be actively carried into the mainstream rather than remaining trapped inside the cavity.

This shift, from closed stagnant vortices at Re = 500 to active ejecting behaviour at Re = 2500, points toward a transition in the surrounding flow behaviour around the dimples. At this Reynolds number, each dimple appears to function as a localized disturbance source, periodically drawing heated fluid outward and disrupting the near-wall flow development, in contrast to the stagnant retention pattern observed at the lower Reynolds number.

c. Re 5000

This section explains the temperature contour and velocity streamline for smooth and dimpled cylindrical container at Re 5000. Showing as follows in the Figure 4.13

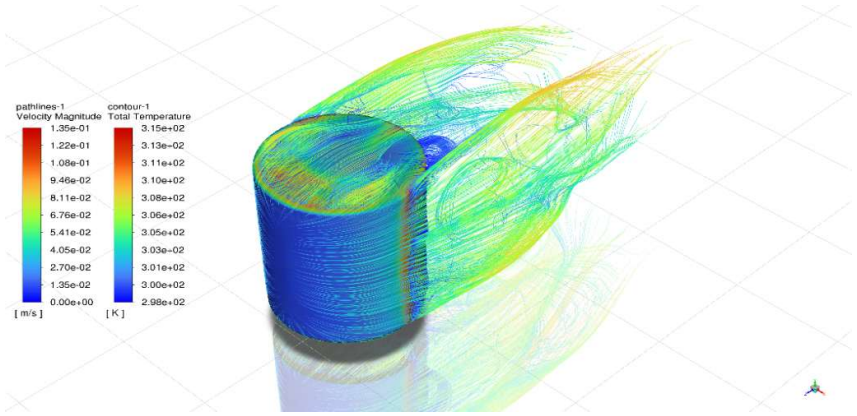

(a)

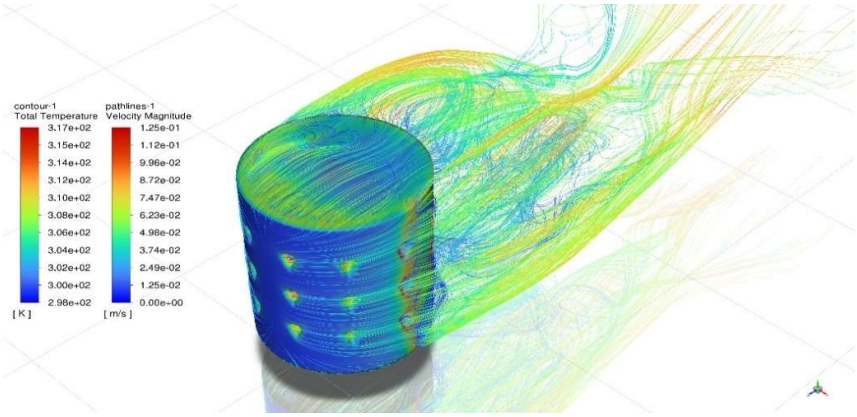

(b)

Figure 4.13 Temperature Contour and Velocity Streamline at Re 5000(a) Smooth Cylinder, (b) Dimpled Cylinder

At Re = 5000, the smooth container exhibits a highly energetic and disordered wake, with large, braided vortical structures persisting well downstream, characteristic of the fully active vortex shedding regime expected at this Reynolds number. The temperature contour remains largely confined to a thin surface layer, with the peak temperature reaching approximately 315 K, indicating that the strong sweeping motion continues to limit heat accumulation at the wall despite the intensified wake turbulence.

For the dimpled container, the pathlines reveal a comparably chaotic and energetic wake, with velocity magnitudes reaching up to 0.125 m/s, closely matching the smooth case. Rather than the isolated, jet-like ejections observed at Re = 2500, the flow around each dimple now appears more tightly integrated into the surrounding turbulent structures, with localized swirling patterns visible at the dimple locations rather than distinctly separated outward bursts. The temperature contour shows the highest local values, reaching approximately 317 K, concentrated at the dimple cavities and along the rear-facing surface, slightly exceeding the peak temperature observed for the smooth container at the same Reynolds number.

This behaviour suggests that as the Reynolds number increases further from 2500 to 5000, the disturbance introduced by each dimple becomes increasingly absorbed into the already highly turbulent boundary layer and wake, rather than standing out as a distinct, separate ejection event. The dimples continue to act as localized sources of near-wall disruption, but their individual contribution becomes less visually distinguishable amid the broader turbulent motion already present at this Reynolds number.

4.8.1.2 Convective heat transfer coefficient

a. Re 500

This section explains the convective heat transfer coefficient contour for smooth and dimpled cylindrical container at Re 500. Showing in the Figure 4.14

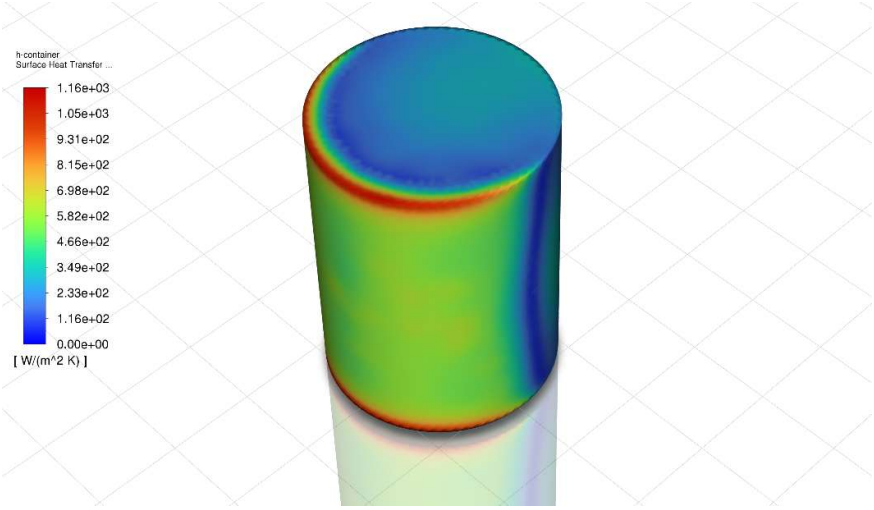

(a)

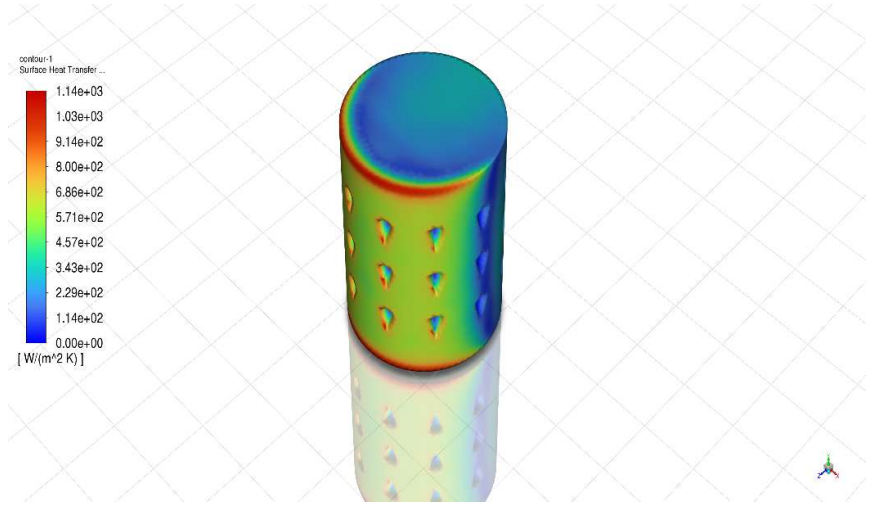

(b)

Figure 4.14 Convective Heat Transfer Coefficient Contour at Re 500 (a) Smooth Cylinder, (b) Dimpled Cylinder

For the smooth container, the highest h values, reaching approximately 1.16×10^{3} W/m²K, are concentrated in a narrow red band near the leading top rim, where the flow first impinges on the surface and the thermal boundary layer remains thinnest. Moving along the cylinder body, h drops progressively into the green-yellow range, before falling sharply to the lowest values, shown in dark blue, along the trailing edge where flow separation occurs and the wake recirculation reduces local convective transport.

For the dimpled container, the overall distribution follows a similar pattern, with peak h of approximately 1.14×10^3 W/m²K concentrated at the leading rim and the lowest values at the trailing edge. However, a clear distinction emerges at each dimple location, where h drops to a localized minimum, appearing as a distinct blue-green patch surrounded by the higher h green-yellow surface. This localized reduction is consistent with the dead-zone behaviour identified earlier, fluid trapped within each dimple cavity at this Reynolds number remains largely stagnant, allowing it to heat up and reducing the wall temperature gradient locally, thereby lowering h precisely at the dimple positions rather than enhancing it.

b. Re 2500

This section explains the convective heat transfer coefficient contour for smooth and dimpled cylindrical container at Re 2500. Showing as follows in the Figure 4.15

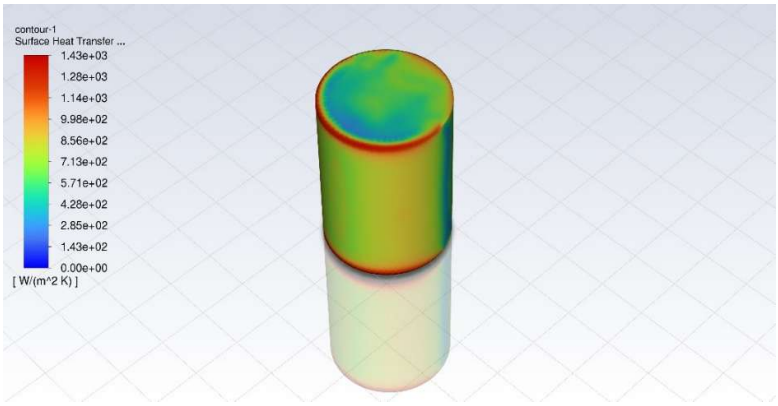

(a)

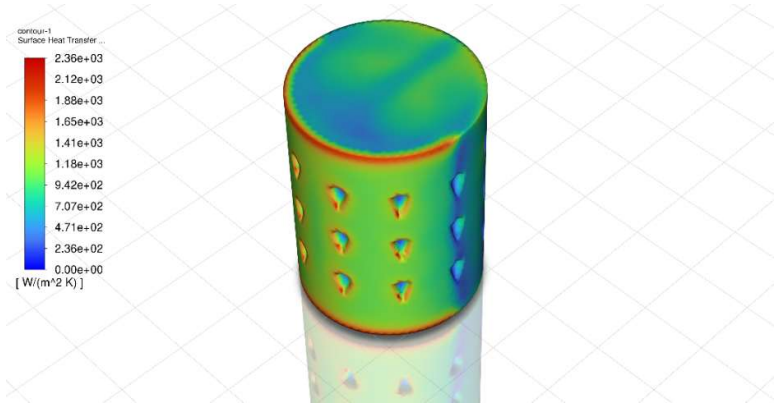

(b)

Figure 4.15 Convective Heat Transfer Coefficient Contour at Re 2500 (a) Smooth Cylinder, (b) Dimpled Cylinder

For the smooth container, the highest h values, reaching approximately 1.43×10^3 W/m²K, remain concentrated in a narrow red band along the leading top rim, consistent with the thinnest boundary layer forming at the point of initial flow impingement. Moving down the cylinder body, h settles into a broad yellow-orange region around 700–850 W/m²K, before dropping to the lowest values, shown in dark blue, along the narrow trailing strip where the wake separates.

For the dimpled container, the peak h rises substantially to approximately 2.36×10^3 W/m²K, again concentrated at the leading rim, considerably higher than the smooth case. More notably, the flat surface between dimples now settles into a higher green band around 940–1180 W/m²K, exceeding the equivalent region on the smooth container. Each dimple is further outlined by a distinct red rim reaching up to 1880–2120 W/m²K, while the dimple interior itself shows a comparatively lower blue-green value around 470–700 W/m²K.

This pattern reflects the ejection behaviour identified in the corresponding pathline analysis, accelerated flow escaping each dimple cavity sharply raises h along the dimple edges, while the cavity interior retains a locally reduced value, though still higher than the stagnant dead-zone condition observed at Re = 500. Combined with the elevated body-averaged h across the flat surface, this indicates that the dimpled geometry now outperforms the smooth container in convective heat transfer at Re = 2500.

c. Re 5000

This section explains the convective heat transfer coefficient contour for smooth and dimpled cylindrical container at Re 5000. Showing as follows in the Figure 4.16

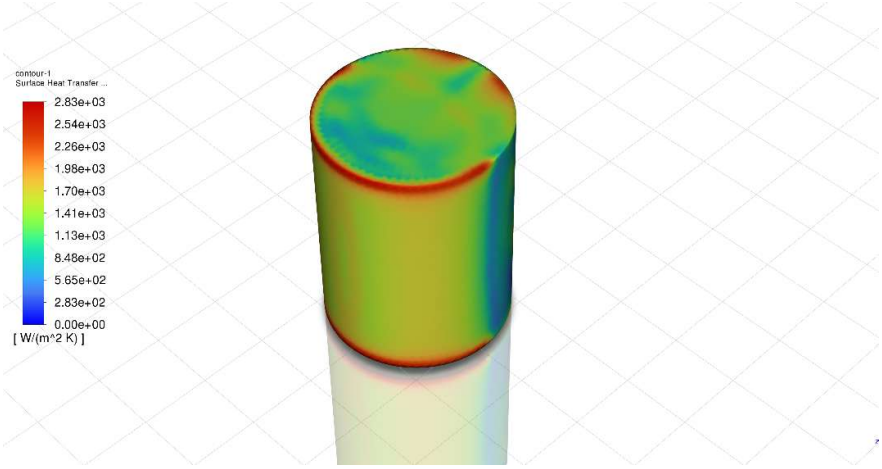

(a)

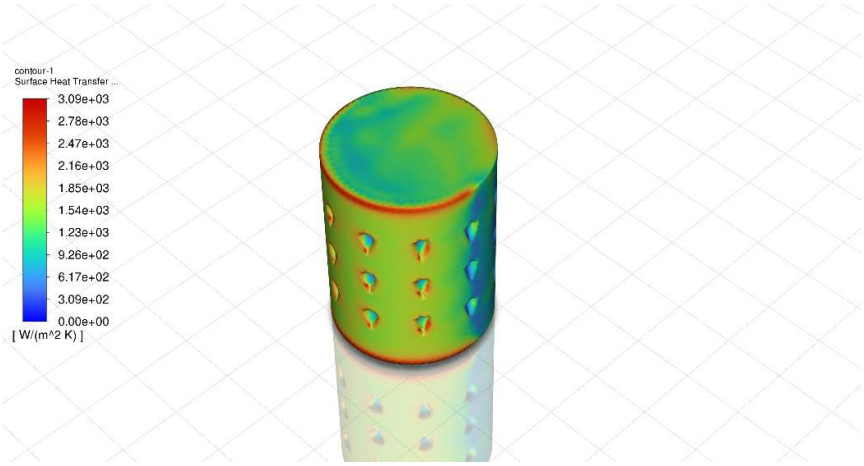

(b)

Figure 4.16 Convective Heat Transfer Coefficient Contour at Re 5000 (a) Smooth Cylinder, (b) Dimpled Cylinder

For the smooth container, the peak h reaches approximately 2.83×10^3 W/m²K, concentrated along the leading top rim as observed in the lower Reynolds number cases. The cylinder body settles predominantly into a broad yellow-green band around 1130–1700 W/m²K, with the surface appearing noticeably more mottled and non-uniform compared to Re = 2500, reflecting the intensified wake turbulence and unsteady flow structures identified in the corresponding pathline analysis. The lowest values remain confined to the narrow trailing strip where flow separation occurs.

For the dimpled container, the peak h increases further to approximately 3.09×10^3 W/m²K, again exceeding the smooth case at the leading rim. The flat surface between dimples settles into a higher band around 1540–2160 W/m²K, consistently above the equivalent smooth-surface region. Each dimple continues to display a distinct red-orange rim reaching up to 2470–2780 W/m²K, while the dimple interior shows comparatively lower values around 620–930 W/m²K, though still considerably higher than the near-stagnant values observed at Re = 500.

d. Time averaged h Smooth cylinder vs dimpled cylinder

Since the LES-based simulation is inherently transient, the instantaneous convective heat transfer coefficient fluctuates continuously with the unsteady wake and vortex shedding behaviour discussed in the preceding sections. To meaningfully compare the thermal performance of the smooth and dimpled surfaces, the instantaneous h values were therefore time-averaged over a statistically stationary period of the simulation, Showing in the Figure 4.17 and Table 3.3

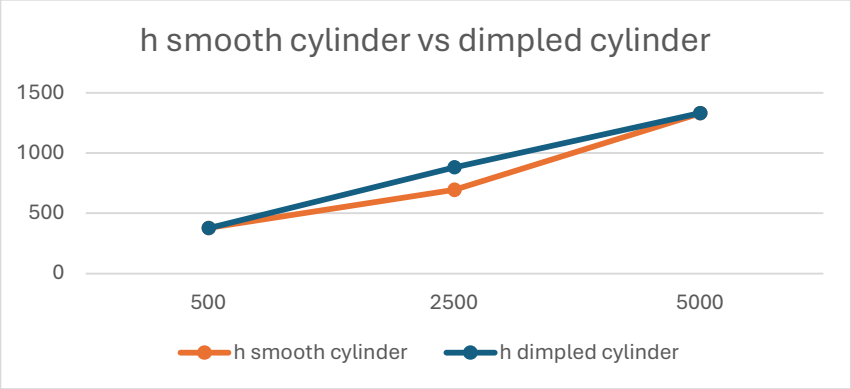

Figure 4.17 Convective Heat Transfer Coefficient Time-Averaged

Table 4.2 Time Average h Smooth Cylinder vs Dimpled Cylinder

Re	h smooth cylinder	h dimpled cylinder
500	378,9893176	377,627517
2500	693,9767696	881,3981524
5000	1329,852526	1330,51299

At Re = 500, the two geometries show nearly identical performance, with h reaching 378.99 W/m²K for the smooth container and 377.63 W/m²K for the

dimpled container, corresponding to the dimpled surface performing marginally lower by only 0.36%. This near-equivalence is consistent with the dead-zone behaviour identified in the earlier contour and pathline analysis, where fluid trapped within each dimple cavity at this low Reynolds number offsets any potential enhancement from the surrounding flat surface, resulting in an overall performance essentially on par with the smooth container rather than a clear improvement.

A markedly different trend emerges at Re = 2500, where h increases to 693.98 W/m²K for the smooth container but rises considerably further to 881.40 W/m²K for the dimpled container, representing a substantial enhancement of 27.01%. This result aligns directly with the ejection-driven mixing mechanism identified previously, in which sufficient flow momentum at this Reynolds number enables fluid to actively escape each dimple cavity, disrupting the near-wall thermal boundary layer and significantly improving convective heat transfer across the dimpled surface.

At Re = 5000, however, the enhancement effectively vanishes, with h reaching 1329.85 W/m²K for the smooth container and 1330.51 W/m²K for the dimpled container, a difference of only 0.05%. Despite the dimpled geometry still exhibiting locally elevated h around each dimple rim in the contour analysis, the already highly turbulent and chaotic wake at this Reynolds number appears to diminish the relative contribution of the dimple-induced disturbance, causing the two geometries to converge toward comparable overall performance.

4.8.2 PCM Melting Result

4.8.2.1 Paraffin wax melting distribution

This section discusses the effect of the dimpled surface on the liquid fraction melting rate of the PCM.

a. Smooth surface PCM

For the smooth surface PCM, the melting contour of liquid fraction showing in the Figure 4.18

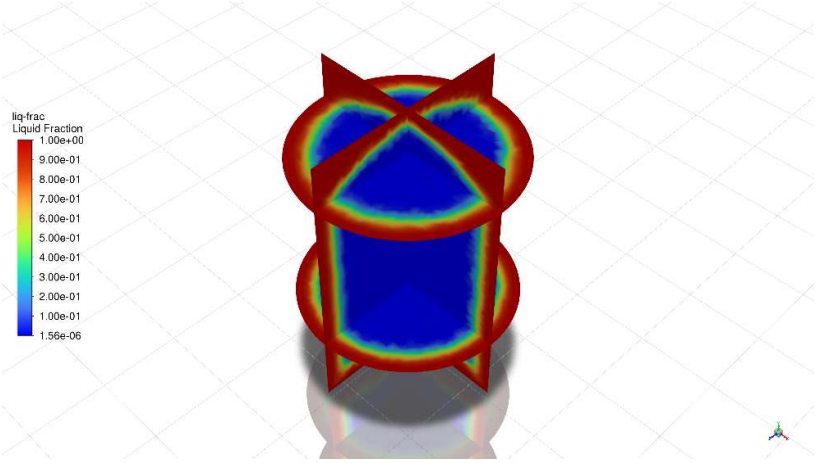
liq-frac
Liquid Fraction
1.00e+00
9.00e-01
8.00e-01
7.00e-01
6.00e-01
5.00e-01
4.00e-01
3.00e-01
2.00e-01
1.00e-01
1.56e-06

(a)

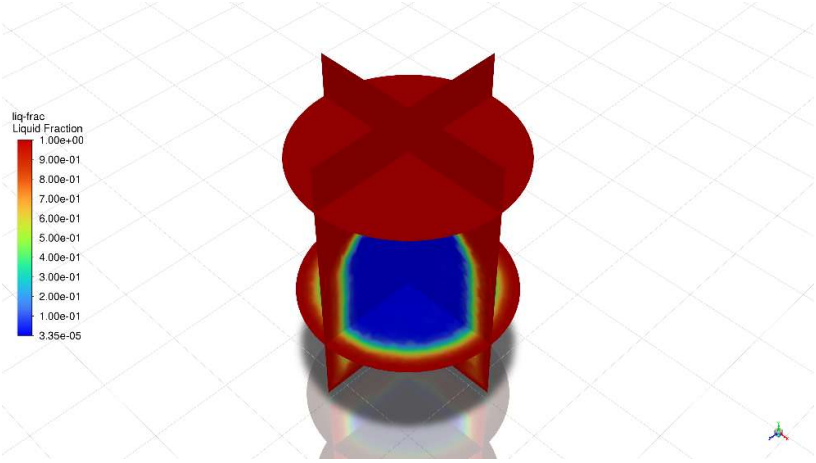
liq-frac
Liquid Fraction
1.00e+00
9.00e-01
8.00e-01
7.00e-01
6.00e-01
5.00e-01
4.00e-01
3.00e-01
2.00e-01
1.00e-01
3.35e-05

(b)


liq-frac
Liquid Fraction
1.00e+00
9.00e-01
8.00e-01
7.00e-01
6.00e-01
5.00e-01
4.00e-01
3.00e-01
2.00e-01
1.00e-01
6.51e-05

(c)

Figure 4.18 Liquid Fraction Contour in a Smooth Surface PCM (a) 300s, (b) 600s, (c) 900s

At t = 300 s, the majority of the cross-section has already transitioned to the fully liquid state, indicated by the extensive red region reaching a liquid fraction of 1.0. A distinct unmelted solid core remains near the center of the container, appearing as a rounded, near-square region with a liquid fraction close to zero, surrounded by a relatively narrow green-yellow transition band representing the mushy zone. The melting front at this stage has progressed fairly uniformly inward from all sides of the container wall, consistent with the radially symmetric heating boundary condition applied to the smooth surface.

By t = 600 s, the solid core has contracted considerably, retaining a broadly similar rounded shape but occupying a visibly smaller fraction of the cross-section. The surrounding mushy zone remains relatively thin, indicating that the melting front continues to advance at a fairly consistent rate as it moves further inward. The persistence of an approximately symmetric core shape suggests that heat is being conducted and convected toward the center in a largely uniform manner around the container circumference.

By t = 900 s, the remaining solid region has diminished further and adopted a more triangular, distorted shape rather than the rounded form observed at earlier times. This shift indicates that natural convection currents within the liquid PCM have begun to influence the melting pattern more strongly as the liquid layer thickens. When the PCM fully melt, it stores 20,02 J/Kg total enthalphy.

b. Teardrop dimpled surface PCM

For the teardrop dimpled surface PCM, the melting contour of liquid fraction showing in the Figure 4.19

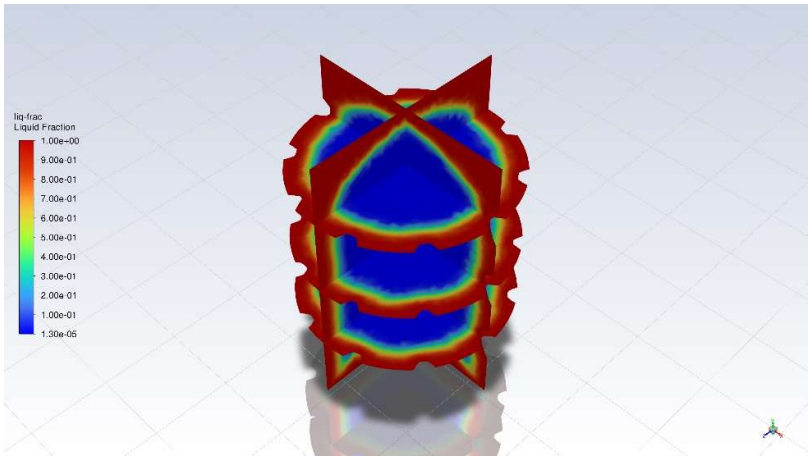
liq-frac
Liquid Fraction
1.00e+00
9.00e-01
8.00e-01
7.00e-01
6.00e-01
5.00e-01
4.00e-01
3.00e-01
2.00e-01
1.00e-01
1.30e-05

(a)

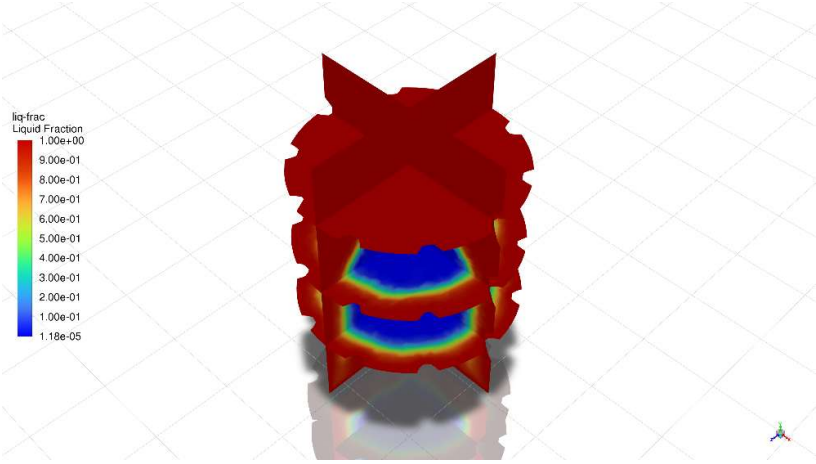
liq-frac
Liquid Fraction
1.00e+00
9.00e-01
8.00e-01
7.00e-01
6.00e-01
5.00e-01
4.00e-01
3.00e-01
2.00e-01
1.00e-01
1.18e-05

(b)


liq-frac
Liquid Fraction
1.00e+00
9.00e-01
8.00e-01
7.00e-01
6.00e-01
5.00e-01
4.00e-01
3.00e-01
2.00e-01
1.00e-01
1.12e-04

(c)

Figure 4.19 Liquid Fraction Contour in a Teardrop Dimpled Surface PCM at Each Flow Time (a) 300s, (b) 600s, (c) 900s

At t = 300 s, the melting pattern differs noticeably from the smooth container case. Rather than a single continuous solid core, the unmelted region appears segmented into three distinct horizontal bands stacked along the container height, each separated by fully melted (red) layers. This banded structure corresponds directly to the three rows of dimples positioned along the container surface, indicating that the locally increased surface area and disrupted near-wall flow at each dimple row accelerate melting preferentially at those elevations, leaving the solid PCM confined to the regions between rows.

By t = 600 s, the topmost solid band has fully melted, leaving only two remaining unmelted regions near the lower half of the container. The remaining solid segments have also contracted in size compared to t = 300 s, though they retain a similarly flattened, elongated shape rather than a rounded core, continuing to reflect the influence of the dimple row spacing on the melting progression.

By t = 900 s, only a single, considerably reduced solid region remains near the bottom of the container, bounded by a narrow mushy zone. The near-complete melting of the upper and middle portions of the container by this stage, compared to the still-substantial solid core observed for the smooth container at the same flow time, suggests that the dimpled surface promotes a faster overall melting rate, consistent with the row-wise melting pattern established from the earliest time instance. When the PCM fully melt, it stores 19,82 J/Kg total enthalphy.

4.8.2.2 Liquid fraction vs flow time

This section discusses the effect of the dimpled surface on the liquid fraction over melting flow time of the PCM. To complement the qualitative contour comparison presented above, the melting progression of the smooth and dimpled containers is further examined by tracking the volume-averaged liquid fraction over the entire flow time, providing a quantitative basis for evaluating the overall melting rate between the two geometries, Showing as follows in the Figure 4.20

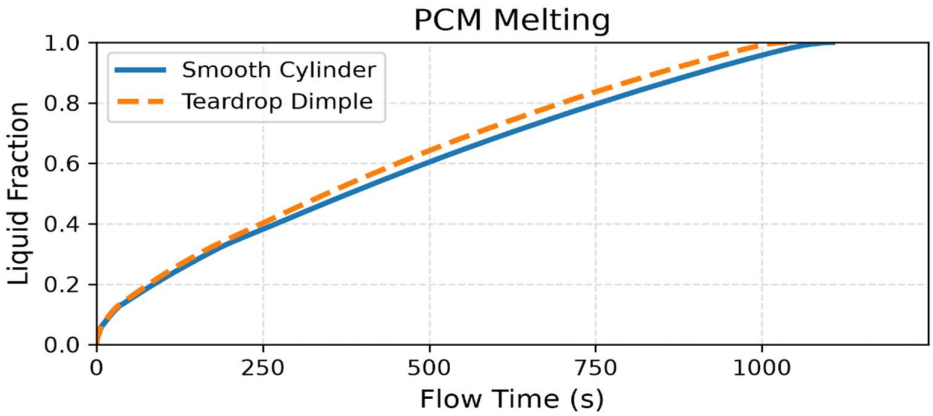

Figure 4.20 Liquid Fraction Flow Time Between Surfaces

Figure 4.20 presents the volume-averaged liquid fraction as a function of flow time for the smooth and teardrop-dimpled containers. Both curves exhibit a similar overall trend, characterized by a rapid initial rise in liquid fraction during the early stage of melting, followed by a more gradual, near-linear increase throughout the majority of the flow time, before tapering off as the liquid fraction approaches unity. This shape reflects the typical conduction-dominated onset of melting near the heated wall, transitioning into a natural convection-driven regime as a sufficient liquid layer develops.

Throughout nearly the entire melting duration, the teardrop-dimpled container maintains a consistently higher liquid fraction than the smooth container at any given flow time, with the orange curve positioned slightly above the blue curve from the early stage onward. This persistent, though modest, offset indicates that the dimpled surface accelerates the overall melting process relative to the smooth container, consistent with the row-wise melting pattern and locally enhanced surface interaction identified in the preceding contour analysis.

As the liquid fraction approaches unity, the two curves gradually converge, with the dimpled container reaching complete melting slightly earlier at approximately 1038 seconds of flow time, compared to 1106 seconds for the smooth container. This confirms that the enhancement observed throughout the melting process translates into a measurable reduction in total melting time for the dimpled geometry.